Journal of Crystal Growth 488 (2018) 16–22

Contents lists available at ScienceDirect

Journal of Crystal Growth

journal homepage: www.elsevier.com/locate/crys

Induction-heating MOCVD reactor with significantly improved heating efficiency and reduced harmful magnetic coupling

Kuang-Hui Li, Hamad S. Alotaibi, Haiding Sun, Ronghui Lin, Wenzhe Guo, Carlos G. Torres-Castanedo, Kaikai Liu, Sergio Valdes-Galán, Xiaohang Li *

King Abdullah University of Science and Technology (KAUST), Advanced Semiconductor Laboratory, Thuwal 23955-6900, Saudi Arabia

ARTICLE INFO

Article history:
Available online 23 February 2018
Communicated by T. Paskova

Keywords:
A1. Computer simulation
A1. Heat transfer
A3. Metalorganic chemical vapor deposition processes
B1. Nitrides
B2. Semiconducting aluminum compounds

ABSTRACT

In a conventional induction-heating III-nitride metalorganic chemical vapor deposition (MOCVD) reactor, the induction coil is outside the chamber. Therefore, the magnetic field does not couple with the susceptor well, leading to compromised heating efficiency and harmful coupling with the gas inlet and thus possible overheating. Hence, the gas inlet has to be at a minimum distance away from the susceptor. Because of the elongated flow path, premature reactions can be more severe, particularly between Al- and B-containing precursors and NH_3. Here, we propose a structure that can significantly improve the heating efficiency and allow the gas inlet to be closer to the susceptor. Specifically, the induction coil is designed to surround the vertical cylinder of a T-shaped susceptor comprising the cylinder and a top horizontal plate holding the wafer substrate within the reactor. Therefore, the cylinder coupled most magnetic field to serve as the thermal source for the plate. Furthermore, the plate can block and thus significantly reduce the uncoupled magnetic field above the susceptor, thereby allowing the gas inlet to be closer. The results show approximately 140% and 2.6 times increase in the heating and susceptor coupling efficiencies, respectively, as well as a 90% reduction in the harmful magnetic flux on the gas inlet.

0. Introduction

Because of its large direct bandgap, AlN is crucial for important ultraviolet (UV) optoelectronics and power electronics applications. However, the growth of high-quality AlN thin films on commercially viable sapphire substrates by metalorganic chemical vapor deposition (MOCVD) has been difficult to realize because it often depends on time-consuming and complex epitaxial lateral overgrowth (ELO) and precursor pulsing schemes [1,2]. Extreme-high-temperature (EHT) (over 1600 °C) growth has been shown to be highly effective for reducing the defect density due to resulting from enhanced Al adatom mobility [3,4], which is also essential for shortening the ELO process [5]. The impurity incorporation can be greatly suppressed at the higher temperatures as well [6]. In addition, hexagonal BN (h-BN) is an emerging material for UV optoelectronics and power electronics. Recently, the growth of high-quality h-BN was demonstrated at 1600 °C or above [7–9]. These studies manifest the potential of EHT growth for Al- and B-containing III-nitride alloys.

Generally, the heating sources of MOCVD reactors include an electric resistant heater and an induction heater. The resistant heater has better temperature uniformity control by employing multi-zone technology. However, it is not ideal for EHT growth because it is not as stable and reliable as the induction heater at higher temperatures because it could soften, gradually become fragile, and eventually break during thermal cycling, even if it does not reach its melting temperature. Furthermore, the susceptor will partially reflect thermal radiation from the resistant heater. Hence, the resistant heater has to be hundreds of degrees higher to reach the target susceptor temperature, which reduces the heating efficiency (Based on discussions with Dr. Gary Tompa (SMI president) and Dr. Ajit Paranjpe (Veeco CTO)). Nevertheless, the majority of high-quality III-nitride alloys, especially the most common, such as InGaN, GaN, and Ga-rich AlGaN, can be grown at relatively low temperatures (<1200 °C) [10–12]. Therefore, the resistant heater has been employed in most commercial MOCVD reactors.

Because of better stability and reliability, the induction heater is the more common heater source for EHT MOCVD reactors. For instance, researchers at North Carolina State University (NCSU) developed a vertical cold-wall MOCVD reactor capable of reaching temperatures over 1800 °C, as shown in Fig. 1 [13–17]. MOCVD

* Corresponding author.
E-mail address: xiaohang.li@kaust.edu.sa (X. Li).

https://doi.org/10.1016/j.jcrysgro.2018.02.031
0022-0248/© 2018 Published by Elsevier B.V.

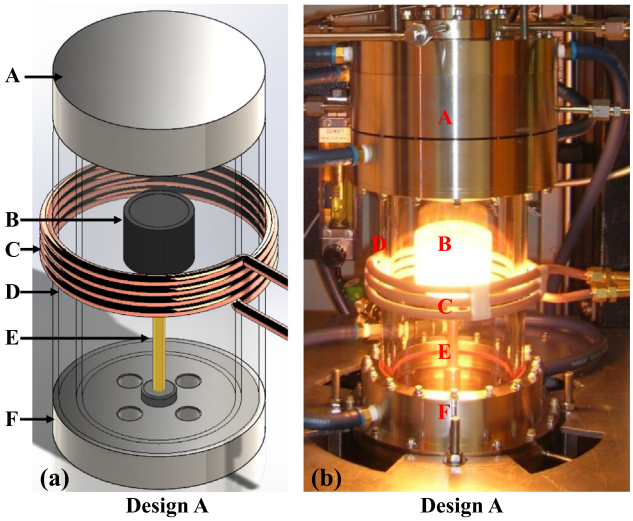

Fig. 1. (a) Isometric view of the conventional induction-heating MOCVD reactor (Design A) and (b) a photograph (courtesy of Prof. Z. Sitar, NSCU) of Design A. A, B, C, D, E, and F represent the gas inlet, susceptor, induction coil, double quartz wall, susceptor supporter, and bottom flange, respectively.

reactors with a similar design are also supplied commercially by various companies [18,19]. In this conventional design, an induction coil is installed outside the quartz chamber to heat up the wafer susceptor. Because of the gap between the coil and the susceptor, there exists an uncoupled magnetic field above the susceptor surface. Not only does the uncoupled magnetic field compromise the heating efficiency, it can also couple with the gas inlet. Specifically, the gas inlets, often made of metallic stainless steel, cannot be too close to the susceptor surface or they will overheat. Because of the resulting longer precursor flow path, this design may lead to considerable premature reactions between NH_3 and Al- and B-containing metalorganics precursors, compromising the material quality and growth efficiency [20–22].

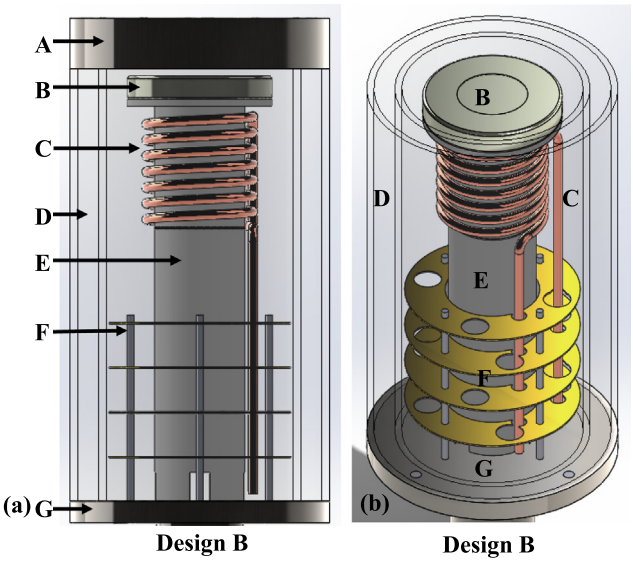

Fig. 2. (a) The side view and (b) isometric view of the proposed design (Design B) without the gas inlet, where A, B, C, D, E, F, and G represent the gas inlet, T-shaped susceptor, induction coil, double quartz wall, supporter, heat shield, and bottom flange, respectively. The thermal insulator separating the coil from the susceptor is not shown here but it is shown in Fig. 3.

In this work, we propose a design to circumvent these issues of conventional induction-heating MOCVD reactors [23]. By introducing a T-shaped susceptor surrounded by the induction coil within the reactor chamber, as shown in Fig. 2, the magnetic flux on the gas inlet can be reduced by almost one order of magnitude thanks to the susceptor's magnetic shielding. Consequently, gas inlets such as a showerhead can be brought closer to the susceptor to minimize premature reactions. Additionally, most of the magnetic flux is utilized for heating, hence improving the overall heating efficiency considerably. Hereinafter, the conventional and proposed designs are referred to as Design A and Design B, respectively.

1. Method and materials

For Design A and Design B, simulation models were constructed to include a susceptor surface that holds a two-inch wafer substrate. Design A employed a 6 cm-diameter and 6-cm-tall cylindrical susceptor, as shown in Fig. 3(a). In reality, the susceptor of the induction-heating MOCVD reactor usually possesses a small hole at the bottom of the rotation spindle. However, the hole should not impact the simulation result considerably and thus it was not included in the modeling for both designs. In Design B, the T-shaped susceptor comprised two major components. As shown in Fig. 3(b), the first component was a 2-in.-diameter and 5-cm-tall cylinder. The second component was an 8.6 cm-diameter and 1-cm-thick plate on top of the susceptor, whose central pocket held the substrate. A 2-in.-diameter and 0.5 mm-thick Al_2O_3 substrate was placed in the pocket. A torus-shaped induction coil with four turns surrounded the cylinder and was situated under the plate. The coil outer diameter was 10 mm and the coil was overshadowed by the plate vertically. For Design A, a thermal insulator layer was installed on the side surface and non-central area of the bottom surface of the susceptor to suppress the thermal radiation. The central area of the bottom surface was not connected to anything. The thermal insulator was configured for Design B in a similar way, but it could also protect the copper coil from strong thermal radiation. To protect the coil from the ambient gas and high temperature in Design B, another thermal insulator can be installed on the outer side of the coil. Because this second thermal insulator did not impact the thermal and magnetic simulation considerably, it was not included in the modeling.

In general, most MOCVD susceptors are made of graphite with a silicon carbide (SiC) coating. However, the SiC coating cannot sustain the EHT for a long time before peeling off (Based on discussion with Dr. K. Balakrishnan based on his high temperature AlN growth experience at Meijo University.) Tungsten, on the other hand, is an inert conductor with a melting point of ~3400 °C [24–28]. It has been utilized for high-temperature nitride growth in the industry [29]. In our simulation, therefore, the T-shaped susceptor was made of tungsten. However, it is noted that tungsten may react with NH_3 at the EHT (based on discussions with Dr. K. Balakrishnan from and Dr. Ajit Paranjpe). [30], which could be addressed by the use of a tantalum carbide (TaC) coating. Alternatively, the tungsten susceptor could be replaced by a sintered TaC susceptor for the EHT MOCVD, albeit at a much higher cost.

The gas inlet was a non-magnetic stainless-steel cylinder with a thickness and diameter of 8 and 17 cm, respectively, which is close to the showerhead for a 2-in. reactor in reality. The gas inlets of both designs were supplied sufficient cooling capacity to maintain them at 10 °C. The gap between the gas inlet and the substrate was 10 mm for Design A and Design B, although the gap for conventional induction-heating MOCVD reactors is much larger due to the harmful induction coupling. It is noted that the gas inlet should comprise non-magnetic materials, which can protect the gas inlet from more

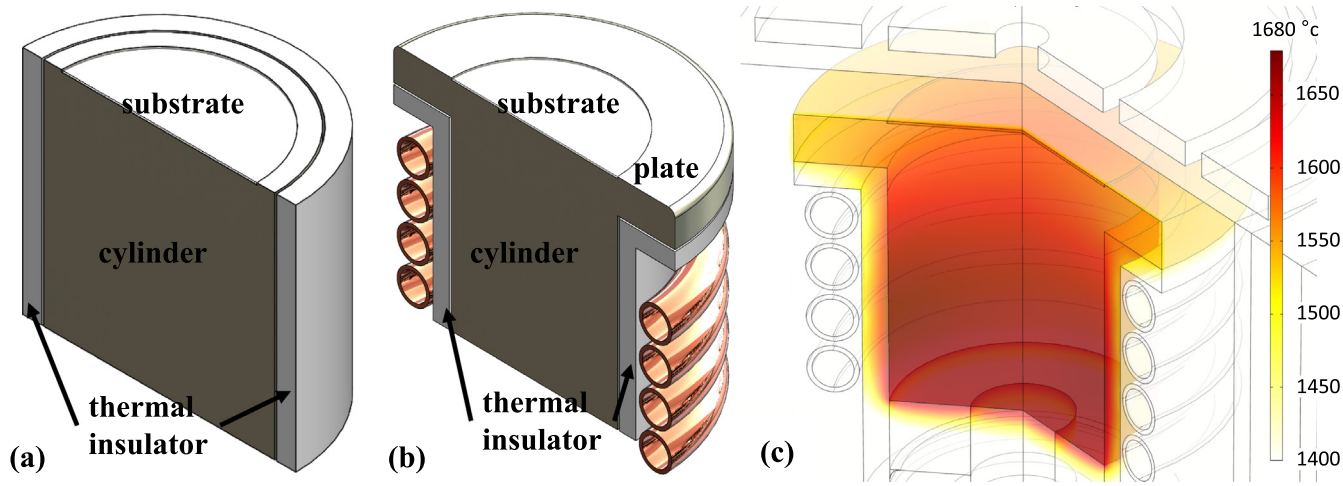

Fig. 3. The susceptors of (a) Design A and (b) Design B, and (c) the temperature gradient of Design B with the substrate temperature at 1600 °C showing the thermal conduction.

enhanced induction coupling as the magnetic materials respond best to induction heating because of the ferromagnetic and ferrimagnetic nature [31,32]. Ferromagnetic and ferrimagnetic materials have long-range spin ordering so that the spin flipping by alternating magnetic field will generate more heat. Such property causes ferromagnetic and ferrimagnetic materials heats up by induction heater more efficient than paramagnetic materials. Most showerheads are made of stainless steel and some stainless steel has ferromagnetic property which is not suitable for making the showerhead. Stainless steel 304 and 316 are austenitic steel and have negligibly responsive to magnetic fields which means that it can be used in applications where a non-magnetic metal is required.

The simulation was conducted using cylindrical symmetry because of the axial symmetry of the susceptor. The numerical calculations were carried by finite element analysis using of COMSOL MultiPhysics 4.3a. The mesh included 23,979 triangular elements and 97,395 degrees of freedom. The heat transfer by thermal radiation, conduction, and induction was simulated by the built-in models [33]. Most commercial induction heaters operate at frequencies of 1–30 kHz. In this work, the frequency was set to be 10 kHz. With the induction heater being on, the cylinders of both designs can couple the magnetic field within the coil to generate heat because of the eddy current. For both designs, the substrates received heat primarily through thermal conduction from the cylinders, as shown in Fig. 3(b). Furthermore, the plate can shield and thus reduce the magnetic field above the plate in Design B as long as the plate thickness is sufficiently large as compared to the skin depth. The detailed configuration of Design A and Design B and the relevant properties of the chosen materials can be found in the supplementary materials.

The mathematical equations for induction heating are based on Maxwell's equations. According to $\vec{J} = \sigma\vec{E}$, $\vec{B} = \vec{\nabla} \times \vec{A}$, and $\vec{E} = -\nabla V - \frac{\partial \vec{A}}{\partial t}$, where σ, $\vec{A}$, and V are the conductivity, magnetic vector potential, and electric potential, respectively, Maxwell–Ampere's law can be further derived as $\vec{\nabla} \times (\vec{\nabla} \times \vec{A}) = \mu_0\mu_r[\vec{J} + \epsilon_0\epsilon_r \frac{\partial}{\partial t}(-\vec{\nabla}V - \frac{\partial \vec{A}}{\partial t})]$, where μ_r is the relative magnetic permeability and ϵ_r is the relative electrical permittivity. Because alternating current was applied, $\vec{E}$, V, and $\vec{A}$ oscillated with the angular frequency of the alternative, current ω, i.e. $\vec{E}(\vec{r},t) = \vec{E}(\vec{r})e^{i\omega t}$, $V(\vec{r},t) = V(\vec{r})e^{i\omega t}$, and $\vec{A}(\vec{r},t) = \vec{A}(\vec{r})e^{i\omega t}$. The induction coil was modeled as s torus shape, meaning $\vec{\nabla}V = \frac{V_{coil}}{2\pi R}\hat{\phi}$, where V_{coil}, R, and $\hat{\phi}$ are the electric potential, the radius of the induction coil, and the unit vector, respectively. Therefore, the governing equation for the induction heating is

$$[\nabla^2 + \mu_0\mu_r(\epsilon_0\epsilon_r\omega^2 - i\sigma\omega)]\vec{A} = \mu_0\mu_r(\sigma + i\epsilon_0\epsilon_r\omega)\frac{V_{coil}}{2\pi R}\hat{\phi} \quad (1)$$

In the simulation, the substrate temperature range was from room temperature to 1900 °C, which corresponds to the induction heater powers of 18.5 and 8 kW for Design A and Design B, respectively. Although the melting point of sapphire is approximately 2000 °C [34], temperatures above 1900 °C may not be practical as sapphire may then be softened or partially melted. Thus, the maximum induction heater powers applied for Design A and Design B in this work were 18.5 and 8 kW, respectively. The substrate temperature of 1600 °C was chosen as the target temperature when the heating efficiency and the harmful coupling were compared in Design A and Design B.

The substrate relied on the heat transfer from the heated cylinder to reach the target substrate temperature for both designs. The heat transfer was modeled by the heat equation and the governing equation is

$$\eta C_P \frac{\partial T}{\partial t} + \eta C_P \vec{u} \cdot \vec{\nabla}T = \vec{\nabla} \cdot (k\vec{\nabla}T) + Q \quad (2)$$

where η is the volumetric mass density, C_P is the specific heat capacity at a constant pressure, T is the absolute temperature, t is the time, k is the thermal conductivity, and Q is the power generated by the eddy current, $Q = \frac{1}{2}Re(\vec{J} \cdot \vec{E})$. Although the susceptor receives energy from the induction coil, it can release heat by convection, conduction, or thermal radiation at any given temperature. Because a large part of the area of the susceptors of both designs was covered by the thermal insulator and the reactor pressure was relatively low (80 mbar), the conduction and convection did not account for the major heat loss of the susceptors. However, the thermal radiation depends on the temperature by the order of four. At the temperatures of interest, the thermal radiation from the susceptor surface dominated the heat loss. The surface-to-ambient thermal radiation was modeled at the boundary and the governing equation was

$$E_b(T) = \varepsilon\xi T^4 \quad (3)$$

At the boundary, $-\vec{n} \cdot \vec{q} = G - J$ and $(1-\varepsilon)G = J - \varepsilon E_b(T)$, where $\vec{n}$ is the normal vector on the boundary, $\vec{q}$ is the radiation heat flux vector, G is the incoming radiative heat flux, J is the total

outgoing radiative heat flux, ε is the emissivity of the material, $E_b(T)$ is the blackbody hemispherical total emissive power, and ξ is the Stefen-Boltzmann constant.

The magnetic flux on the gas inlet directly indicates the degree of harmful induction coupling. High magnetic flux means the gas inlet has excessive harmful coupling and vice versa. The magnetic flux on the gas inlet was calculated, in particular, on the bottom surface (A_1) and lateral surface (A_2) of the gas inlet. The magnetic flux on the top surface of the gas inlet was negligible and thus not considered. By definition, the magnetic flux of a closed surface is $\Phi = \oiint \vec{B}(\vec{r}) \cdot d\vec{A}$. The magnetic flux on the bottom surface (A_1), $d\vec{A}_1 = rdrd\phi\hat{z}$, of the gas inlet, Φ_{bottom}, was calculated by $\Phi_{bottom} = \int_0^{2\pi}\int_0^R B(r)rdrd\phi = 2\pi\int_0^R B(r)rdr$, where R is the radius of the gas inlet. The magnetic flux on the lateral surface (A_2), $d\vec{A}_2 = Rd\phi dz\hat{r}$, of the gas inlet, $\Phi_{lateral}$, was calculated by $\Phi_{lateral} = \int_0^{2\pi}\int_0^H B(z)Rdzd\phi = 2\pi R\int_0^H B(z)dz$, where H is the thickness of the gas inlet. Thus, the total magnetic flux is $\Phi_{total} = \Phi_{bottom} + \Phi_{lateral}$.

2. Results

2.1. Heating efficiency

The heating efficiency is reflected by the equilibrium substrate temperature at given induction heater powers. As shown in Eq. (3), the thermal radiation is strongly dependent on the temperature. Thus, the only way to boost the equilibrium temperature and thus enhance the heating efficiency is to transfer more energy from the induction coil to the susceptor.

As shown in Fig. 4, the substrate temperature of Design B was considerably higher than that of Design A at any given heater power. For instance, Design B achieved 1600 °C at 5 kW, whereas Design A reach only approximately 1080 °C at 5 kW. In fact, Design A required approximately 2.4 times more power, i.e., 12 kW, to reach 1600 °C. Therefore, Design B was 140% $\left(\left[\left(\frac{12-5}{5}\right) - 1\right] \times 100\%\right)$ more efficient than Design A. With a significantly higher heating efficiency, Design B can greatly decrease power consumption. Moreover, Design B can reduce the cost, footprint, and complexity of the induction heater system considerably because these factors are usually proportional to the maximum power of the system. In addition, the heating efficiency of resistive heater is also compared with Design A and Design B. Design A requires 12 kW to reach 1600 °C, and in the resistive heater case it requires 8 kW for reaching 1600 °C. However, Design B only requires 5 kW to reach the same temperature. The simulation proves that the Design B has better heating efficiency than the Design A and resistive heater case.

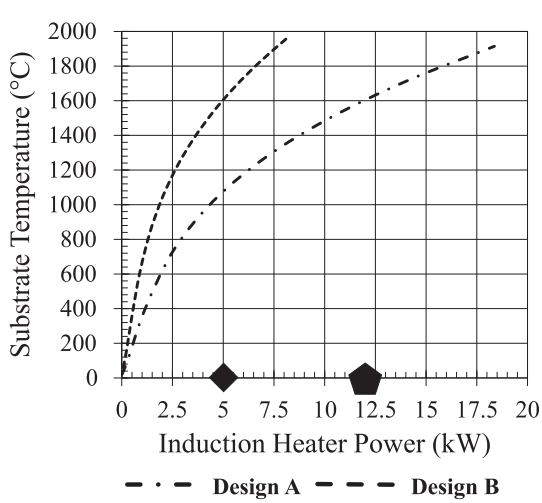

Fig. 4. The substrate temperature versus the induction heater power. The pentagon and the rhombus indicate the required induction powers for reaching the substrate temperature of 1600 °C in Design A and Design B, respectively.

2.2. Harmful coupling

Fig. 5 depicts the magnetic flux density when the substrate temperature of Design A and Design B was 1600 °C. For both designs, the highest density was concentrated around the coil. However, the overall distribution of the contours was remarkably different. For Design A, the contours were sparse away from the coils. This indicates that a considerable part of the energy dissipated in the free space and thus was wasted. In addition, the magnetic flux density on the bottom and side surface of the gas inlet was noticeably as large as that on the susceptor. Because the gas inlet is usually made of metal, it may be overheated, which can cause precursor molecule decomposition within the gas inlet and severe damage to the gas inlet without sufficient cooling. This is the primary reason why a close gas inlet could not be used for the conventional induction-heating MOCVD reactor. For Design B, the contours were mostly confined by the susceptor. There was little magnetic flux in the free space or on the bottom and side surface of the gas inlet, indicating less harmful and wasteful coupling as compared to Design A.

To quantify the magnetic flux on the gas inlet, the magnetic flux density from Fig. 5 was integrated over A_1 and A_2. As shown in Fig. 6, the magnetic fluxes on the gas inlet of Design A and Design B increased continuously with increasing induction heater power, albeit with drastically different slopes. Overall, the gas inlet of Design A received significantly more magnetic flux than Design B by approximately one order of magnitude. This means that Design B had much better magnetic shielding, which is attributed to the introduction of the T-shaped susceptor. Because the induction coil was beneath the plate, the magnetic field generated by the induction coil could hardly penetrate the plate, thereby preventing the harmful coupling with the gas inlet above the susceptor. Such a design alleviates the possibility of overheating the gas inlet and thus reduces the cooling load. It also prevents the precursor decomposition within the gas inlet. Moreover, it makes the close-distance gas inlet feasible, such as in the form of a showerhead-type gas inlet, which is widely deployed, because of its low precursor premature reaction characteristics [35–38].

To quantify the heating due to the coupling, the heating power on the susceptor and the gas inlet of Design A and Design B were calculated and the results are shown in Fig. 7. As exhibited in Fig. 7(a) for Design A, the heating powers on the susceptor and the gas inlet were comparable. At the heater power of 12 kW, which led to the 1600 °C substrate temperature, the heating powers were on the scale of kilowatts meaning that both the susceptor and the gas inlet had strong induction coupling. Around 30% and 15% of the heater power was transferred to the susceptor and the gas inlet, respectively, indicating that the gas inlet would require tremendous cooling power. The rest of the remaining 55% was wastefully released to the surrounding open space, consistent with the analysis of Fig. 5(a). In contrast, for Design B, as shown in Fig. 7 (b), the heating power on the susceptor was almost three orders of magnitude larger than the heating power on the gas inlet, implying that the gas inlet had a weak coupling. Specifically, approximately 80% of the heater power was utilized on the susceptor at the induction heating power of 5 kW, corresponding to the 1600 °C substrate temperature. Less than 20% of the heater power was transferred to the gas inlet and released to the surrounding open space. As also shown in Fig. 7, the susceptor coupling efficiency

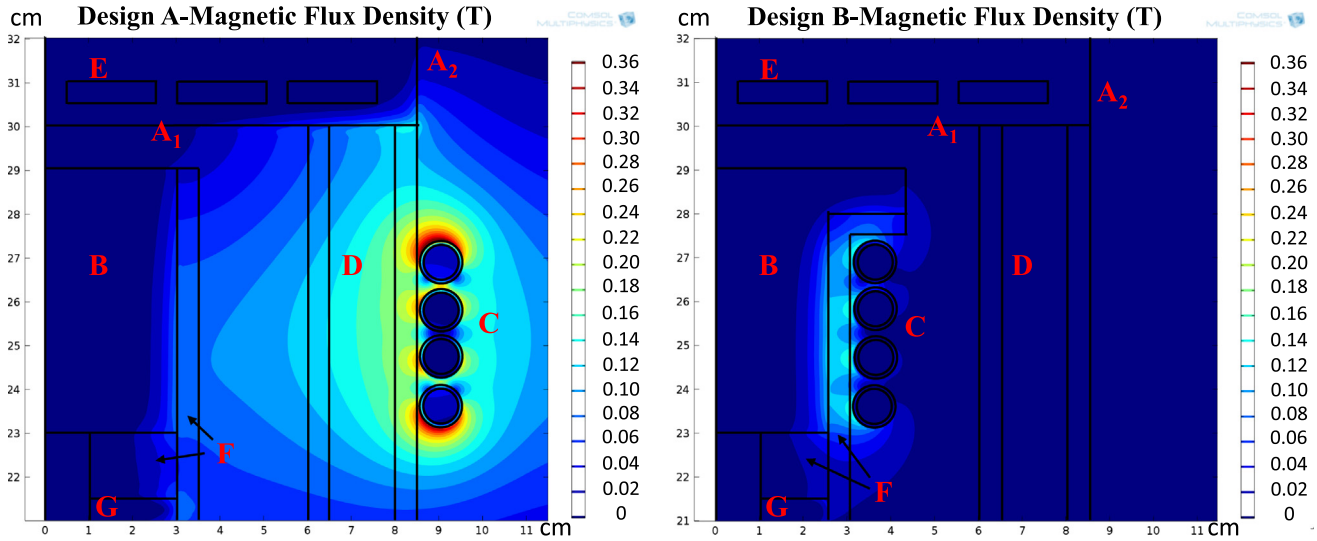

Fig. 5. Cross-sectional view of the magnetic flux density of (a) Design A and (b) Design B at 1600 °C, where B, C, D, E, F, and G represent the susceptor, induction coil, double quartz wall, cooling water channel, thermal insulator, and supporter respectively. A_1 and A_2 are the bottom surface and lateral surface of the gas inlet, respectively.

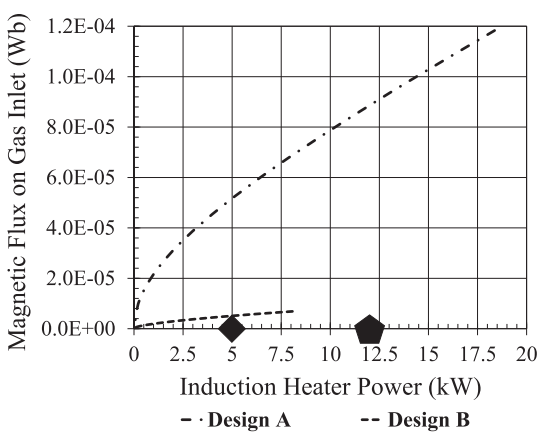

Fig. 6. The magnetic flux on the gas inlet versus the induction heater power. The pentagon and the rhombus indicate the required induction power for reaching the substrate temperature of 1600 °C in Design A and Design B, respectively.

of Design B which is the ratio between the power on the susceptor and the induction heater power, ranged from 55 to 85%, whereas that of Design A was 8 to 32%. At the substrate temperature of 1600 °C, the susceptor coupling efficiency was 2.6 $\left(\frac{82\%}{30\%}\right)$ times higher than that of Design A. Regarding the temperature of the gas inlet, a Thomas-Swan type showerhead has been modeled by CFD. The showerhead has three plenums: the top two plenums are for precursors and the bottom plenum is for the cooling water channel. Under substrate temperature of 1900 °C and 10 mm gap between showerhead and substrate, the simulations show the top plenum is around 30 °C and the bottom plenum temperature is below 200 °C with 40 cc/s cooling water input. The temperature of the cooling water inlet is 10 °C and the outlet temperature is about 30 °C. The cooling capacity is around 3.4 kW, which is close to the thermal radiation power of the top surface of the T-shaped susceptor given the emissivity of 0.4 for polished tungsten surface at high temperature. Thus, the precursors will not decompose considerably before being injected into the reactor.

Although the proposed design (Design B) is aimed at the EHT MOCVD process, it is important to note that it can be employed

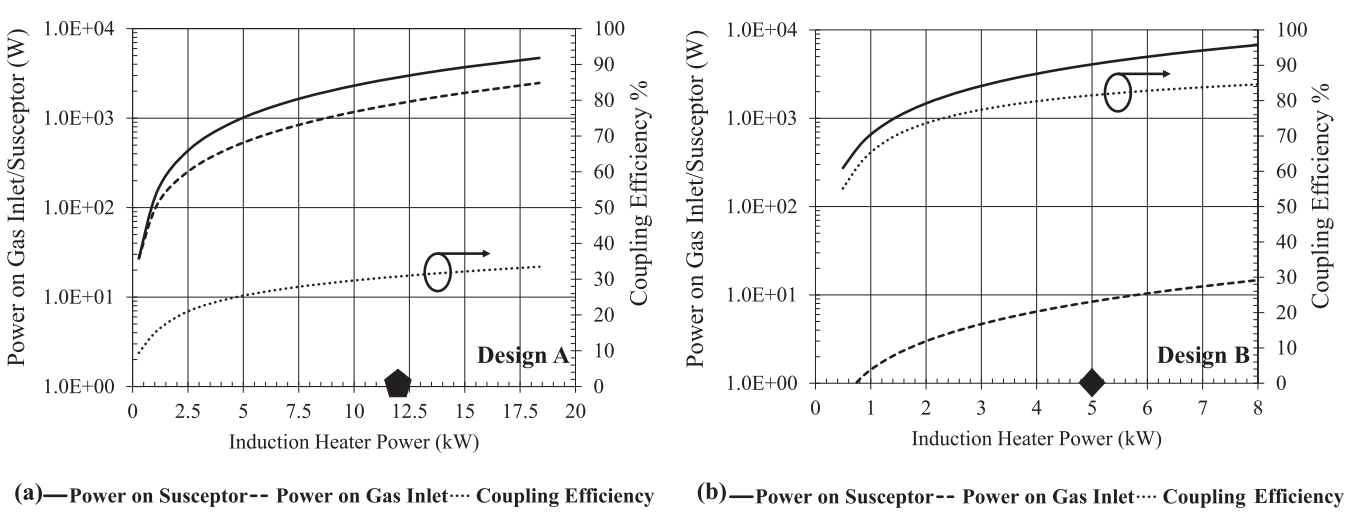

Fig. 7. The induction heater power coupled to the susceptor and gas inlet versus the induction heater power and the susceptor coupling efficiency of (a) Design A and (b) Design B. The pentagon and the rhombus indicate the required induction powers for reaching the substrate temperature of 1600 °C in Design A and Design B, respectively.

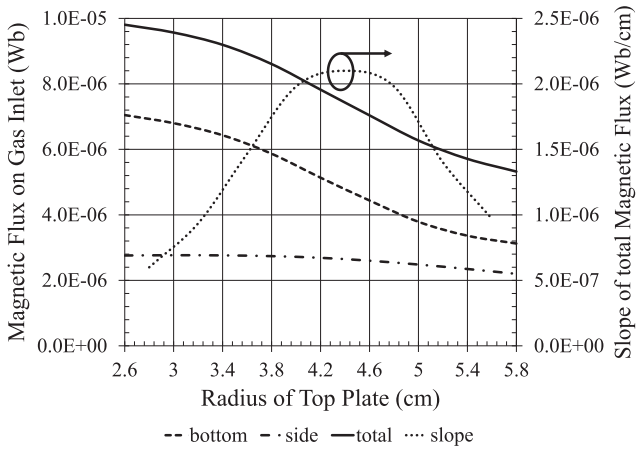

Fig. 8. The magnetic flux on the gas inlet versus the radius of the susceptor plate in Design B.

at lower temperatures as well, such as below 1300 °C for the epitaxy of high-quality Al-rich AlGaN materials and structures [15,39]. This is because the advantages of Design B over Design A are still profound at lower temperatures because it enables the use of the close-distance showerhead for reduced premature reactions. In addition, the heater of Design B would be less expensive and complex to maintain as compared to a conventional reactor with a resistant heater at lower temperatures.

2.3. Control of magnetic shielding in Design B

The magnetic shielding in Design B can be further controlled by deliberately varying the radius of the top plate of the T-shaped susceptor. As shown in Fig. 8, the total magnetic flux on the gas inlet was reduced by 40% when the radius of the top plate was increased from 2.6 to 5.8 cm. In particular, the magnetic flux on the bottom surface of the gas inlet was sensitive to the radius of the top plate, generally following the same trend as the total magnetic flux. In comparison, the magnetic flux on the lateral surface barely changed and was considerably weaker. This indicates that the magnetic shielding mainly reduced the magnetic flux on the bottom surface because the coupling between the induction coil and the side surface of the gas inlet was weak due to magnetic shielding by the T-shaped susceptor in Design B, which was not the case for Design A, as shown in Fig. 5. Theoretically, the radius of the top plate can be further increased, which would further reduce the harmful magnetic coupling. However, there are drawbacks because the substrate temperature would drop with deteriorated substrate temperature uniformity due to the longer thermal conduction path. By taking the first derivative of the total magnetic flux in Fig. 8, the maximum slope occured at 4.3 cm, which means that maximum marginal benefit of the magnetic shielding by increasing the radius of the top plate occurred when the radius was 4.3 cm. In addition, changing the top plate thickness would not impact the magnetic shielding much because the skin depth of tungsten was 3.67 mm at 1600 °C and the plate thickness was 10 mm in this study.

3. Conclusion

An induction-heating MOCVD reactor design was proposed to improve the heating efficiency and reduce the harmful induction coupling with the gas inlet. Specifically, the induction coil surrounded the vertical cylinder of a T-shaped susceptor, which comprised a cylinder and a top plate holding the substrate. The cylinder coupled most of the magnetic field and transferred the heat to the plate; the uncoupled magnetic field was blocked significantly by the plate. Thus, a close gas inlet such as a showerhead for reduced premature reactions was feasible. The simulation results showed approximately 140% and 2.6 times increases in the heating and susceptor coupling efficiencies, respectively, with a 90% reduction in the harmful magnetic flux on the gas inlet. Furthermore, the harmful coupling on the gas inlet could be reduced by deliberately controlling the diameter of the top plate. The proposed design could be applicable for low-cost and low-premature-reaction MOCVD reactors operating at both high and low temperatures.

Acknowledgements

Because of competition and the resulting confidentiality, there is little information on induction-heating MOCVD reactor design available in print and on the internet. We thus appreciate the following people who have generously provided suggestions and advice: Dr. G. Tompa and the engineers at Structured Materials Industries, Dr. K. Balakrishnan at BRIDGE, Dr. J. Creighton at Sandia National Laboratories, Prof. Z. Sitar and Prof. R. Collazo at North Carolina State University, Dr. A. Paranjpe at Veeco Instruments, Mr. J. Schmitt at Nitride Solution, Dr. A. Boyd at AIXTRON, and Prof. S. Novikov at the University of Nottingham. This research was sponsored by the KAUST Baseline Fund BAS/1/1664-01-01 and Equipment Fund BAS/1/1664-01-07.

Appendix A. Supplementary material

Supplementary data associated with this article can be found, in the online version, at https://doi.org/10.1016/j.jcrysgro.2018.02.031.

References

[1] M. Imura, K. Nakano, G. Narita, N. Fujimoto, N. Okada, K. Balakrishnan, M. Iwaya, S. Kamiyama, H. Amano, I. Akasaki, T. Noro, T. Takagi, A. Bandoh, J. Cryst. Growth 298 (2007) 257.
[2] Z. Chen, R. Fareed, M. Gaevski, V. Adivarahan, J. Yang, A. Khan, J. Mei, F. Ponce, Appl. Phys. Lett. 89 (2006) 081905.
[3] N. Fujimoto, T. Kitano, G. Narita, N. Okada, K. Balakrishnan, M. Iwaya, S. Kamiyama, H. Amano, I. Akasaki, K. Shimono, T. Noro, Phys. Status Solidi C 3 (2006) 1617.
[4] Z. Chen, D. Lu, H. Yuan, P. Han, X. Liu, Y. Li, X. Wang, Y. Lu, Z. Wang, J. Cryst. Growth 235 (2002) 188.
[5] M. Imura, K. Nakano, T. Kitano, N. Fujimoto, G. Narita, N. Okada, K. Balakrishnan, M. Iwaya, S. Kamiyama, H. Amano, I. Akasaki, K. Shimono, T. Noro, T. Takagi, A. Bandoh, Appl. Phys. Lett. 89 (2006) 221901.
[6] M. Imura, H. Sugimura, N. Okada, M. Iwaya, S. Kamiyama, H. Amano, I. Akasaki, A. Bandoh, J. Cryst. Growth 310 (2008) 2308.
[7] M. Crawford, A. Allerman, T. Beechem, T. Ohta, D. Medlin, C. Spataru, A. Rice, J. Figiel, M. Smith, International Workshop on Nitride (IWN), Orlando, FL, USA, October 2016.
[8] Y. Cho, A. Summerfield, A. Davies, T. Cheng, E. Smith, C. Mellor, A. Khlobystov, C. Foxon, L. Eaves, P. Beton, S. Novikov, Sci. Rep. 7 (2017) 46799.
[9] T. Cheng, A. Davies, A. Summerfield, Y. Cho, I. Cebula, R. Hill, C. Mellor, A. Khlobystov, T. Taniguchi, K. Watanabe, P. Beton, C. Foxon, L. Eaves, S. Novikov, J. Vac. Sci. Technol. B 34 (2016) 2.
[10] S. Nakamura, T. Mukai, M. Senoh, Appl. Phys. Lett. 64 (1994) 1687.
[11] H. Hirayama, S. Fujikawa, N. Noguchi, J. Norimatsu, T. Takano, K. Tsubaki, N. Kamata, Phys. Status Solidi A 206 (2009) 1176.
[12] J. Zhang, H. Wang, W. Sun, V. Adivarahan, S. Wu, A. Chitnis, C. Chen, M. Shatalov, E. Kuokstis, J. Yang, M. Khan, J. Electron. Mater. 32 (2003) 364.
[13] S. Mita, R. Collazo, A. Rice, R. Dalmau, Z. Sitar, J. Appl. Phys. 104 (2008) 013521.
[14] A. Rice, R. Collazo, J. Tweedie, J. Xie, S. Mita, Z. Sitar, J. Cryst. Growth 312 (2010) 1321.
[15] I. Bryan, Z. Bryan, M. Bobea, L. Hussey, R. Kirste, R. Collazo, Z. Sitar, J. Appl. Phys. 116 (2014) 133517.
[16] Z. Bryan, I. Bryan, S. Mita, J. Tweedie, Z. Sitar, R. Collazo, Appl. Phys. Lett. 106 (2015) 232101.
[17] J. Creighton, M. Coltrin, J. Figiel, J. Cryst. Growth 464 (2017) 132.
[18] http://agnitron.com/ (Jan 22th, 2018).
[19] http://www.qdjason.com/ (Jan 22th, 2018).

[20] D. Zhao, J. Zhu, D. Jiang, H. Yang, J. Liang, X. Li, H. Gong, J. Cryst. Growth 289 (2006) 72.
[21] J. Creighton, G. Wang, W. Breiland, M. Coltrin, J. Cryst. Growth 289 (261) (2004) 204.
[22] C. Chen, H. Liu, D. Steigerwald, W. Imler, C. Kuo, M. Craford, J. Electron. Mater. 25 (1996) 1004.
[23] X. Li, K.-H. Li, H. A. Alotaibi, U.S. Provisional Patent Application # 62396679.
[24] H. Shinno, M. Kitajima, M. Okada, J. Nucl. Mater. 155 (1989) 290.
[25] J. Ohmori, T. Kobayashi, M. Yamada, H. Iida, T. Horie, Fusion Eng. Des. 9 (1989) 207.
[26] F. Incropera, D. Dewitt, Fundamentals of Heat Mass Transfer, second ed., pp. 759.
[27] I. Smid, M. Akiba, M. Araki, S. Suzuki, K. Satoh, Material and Design Considerations for the Carbon Armored ITER Divertor, July 1993.
[28] D. Smith, W. Daenner, Y. Gohar, ITER Blanket, Shield and Material Data Base, 1991.
[29] www.nitridesolutions.com (Jan 22th, 2018).
[30] Y. Peng, P. Dawson, J. Chem. Phys. 54 (1971) 950.
[31] M. Feliachi, G. Develey, IEEE IEEE T. Magn. 27 (1991) 5235.
[32] O. Lucia, P. Maussion, E. Dede, J. Burdio, I.E.E.E.T. Ind, Electron. 61 (2014) 2509.
[33] COMSOL Multiphysic® User's Guide VERSION 4.3.
[34] P. Pradyot, Handbook of Inorganic Chemicals, vol. 529, 2003.
[35] S. Hu, S. Liu, Z. Zhang, H. Yan, Z. Gan, H. Fang, J. Cryst. Growth 415 (2015) 72.
[36] A. Behrends, B. Andrey, W. Andreas, Microelectron. J. 40 (2009) 280.
[37] X. Li, S. Wang, H. Liu, F. Ponce, T. Detchprohm, R. Dupuis, Phys. Status Solidi B 254 (2017) 1600749.
[38] X. Li, S. Wang, Y. Wei, H. Xie, T. Kao, M. Satter, S. Shen, P. Yoder, T. Detchprohm, R. Dupuis, A. Fischer, F.A. Ponce, Phys. Status Solidi B 252 (2015) 2.
[39] X. Li, H. Xie, J. Ryou, F. Ponce, T. Detchprohm, R. Dupuis, Appl. Phys. Lett. 107 (2015) 241109.